Science Advances

AAAS

advances.sciencemag.org/cgi/content/full/3/12/eaao5520/DC1

Supplementary Materials for

Deep tissue optical focusing and optogenetic modulation with time-reversed ultrasonically encoded light

Haowen Ruan, Joshua Brake, J. Elliott Robinson, Yan Liu, Mooseok Jang, Cheng Xiao, Chunyi Zhou, Viviana Gradinaru, Changhuei Yang

Published 8 December 2017, *Sci. Adv.* **3**, eaao5520 (2017)
DOI: 10.1126/sciadv.aao5520

This PDF file includes:

- method S1. Calculation of the focal spot size of TRUE and conventional focusing.
- method S2. Viral injection surgery.
- method S3. Electrophysiological recordings.
- method S4. Daily alignment procedure.
- fig. S1. Setup.
- fig. S2. Electrical signal flow diagram.
- fig. S3. Ultrasound pulse-echo image of the tip of the glass pipette electrode.
- fig. S4. Electrophysiological photocurrent traces from neurons in 500- and 300-μm-thick acute brain slices.
- fig. S5. Electrophysiological photocurrent and membrane voltage traces comparing ultrasound on and off conditions.

Supplementary Materials

method S1. Calculation of the focal spot size of TRUE and conventional focusing.

To calculate the focal spot size of TRUE focusing from the images captured with the observation camera (Camera2 in fig. S1), the image was first cropped to a region (82 × 82 pixels) surrounding the focus profile, and was low-pass filtered by a 3 × 3 averaging filter to smooth the speckle. Then, the focus profile was fit using a 2D Gaussian function $f(x,y) = A\exp\left\{-\left[(x-x_0)^2+(y-y_0)^2\right]\Big/\left(2\sigma^2\right)\right\}+B$, where A, B, x_0, y_0, σ are the fitting parameters. The full width at half maximum (FWHM) focal spot size was obtained by FWHM = $2\sqrt{2\ln 2}\sigma$. The focal spot size of the conventional focusing was calculated in a similar way. However, since the focal spot size was much larger than that of TRUE focusing, the fitting was applied to a region composed of 1040 × 1392 pixels.

method S2. Viral injection surgery.

Mice were anesthetized with an isoflurane gas/carbogen mixture and placed to a stereotaxic frame (David Kopf Instruments, CA, USA). After sterilizing the skin with chlorohexidine, a midline incision was made with a sterile scalpel, the skull surface was cleaned with autoclaved cotton swabs, and the bregma and lambda were identified and leveled to be on the same z-axis. AAV-DJ-CaMKII-bReaChES-TS-YFP (500 nL) was injected into the prelimbic cortex (AP + 1.65 mm, ML ± 0.2 mm, DV − 2.25 mm) using a blunt 35-gauge microinjection needle within a 10 µL microsyringe (NanoFil, World Precision Instruments, FL, USA), which was controlled by a microsyringe pump (UMP3, World Precision Instruments) connected to a controller (Micro4, World Precision Instruments). Following injection, the needle/syringe was held in the same location for an additional 10 min to allow further diffusion. To prevent potential backflow, the needle/syringe was slowly withdrawn over approximately 10 min. After infusion, the scalp was sutured and the mouse was returned to the vivarium for post-operative recovery. Animal husbandry and all experimental procedures involving animal subjects were approved by the Institutional Animal Care and Use Committee (IACUC) and by the Office of Laboratory Animal Resources at the California Institute of Technology under IACUC protocol 1650.

method S3. Electrophysiological recordings.

Mice expressing CaMKII-bReaChES-TS-YFP were euthanized with carbon dioxide and transcardially perfused with ice-cold sucrose-based cutting solution saturated with 95% O_2/5% CO_2 (carbogen) that contained (mM) 85 NaCl, 75 sucrose, 2.5 KCl, 1.25 NaH_2PO_4, 4.0 $MgCl_2$, 0.5 $CaCl_2$, 24 $NaHCO_3$ and 25 glucose. The brain was removed and 300–800 µm thick coronal slices that contained the mPFC were prepared in oxygenated cutting solution using a vibratome (VT-1200, Leica Biosystems, IL, USA). Slices were recovered at 32°C for one hour prior to recording in carbogenated ACSF containing (mM): 125 NaCl, 2.5 KCl, 1.2 NaH_2PO_4, 1.2 $MgCl_2$, 2.4 $CaCl_2$, 26 $NaHCO_3$, and 11 glucose. Slices were transferred to the recording chamber and perfused (1.5 – 2.0 mL/min) with carbogen-saturated ACSF at 32 ± 0.5°C. Whole-cell patch clamp recordings were obtained using a Heka EPC 10 USB amplifier/digitizer (Heka Electronik, Germany) with data sampled at 10 kHz and filtered at 2 kHz. Patch electrodes had resistance of 4 – 8 MΩ and were filled with a potassium gluconate intrapipette solution (mM): 135 K gluconate, 5 KCl, 5 EGTA, 0.5 CaCl2, 10 HEPES, 2 Mg-ATP, and 0.1 GTP.

method S4. Daily alignment procedure.

Before operation each day, the system was tuned to maintain optimal performance of the digital optical phase conjugation (DOPC) system by ensuring fine pixel-to-pixel alignment between the camera and the SLM. This procedure was conducted using the quality assurance (QA) arm of the system by opening shutters SH1 and SH2 as shown in fig. S1. The following steps were performed for the daily alignment.

1. **Playback beam normal to SLM.** To ensure the SLM was perpendicular to the sample and playback beam (S/PB), we enabled the flip mirror FM and tilted the SLM to maximize the intensity measured by the QA photodiode (PD2).
2. **Record and playback a scattering field from QA path for DOPC loop B.** We disabled flip mirror FM and optimized the alignment of DOPC loop B, which was enabled by setting the shutters BSS2 and BSS3 (fig. S1B). This allows the QA light beam to interfere with the reference beam (R), so the phase map of the scattered light could be measured using four-step phase-shifting holography. After measuring the phase map, the conjugate phase map was displayed on the SLM, so the playback beam would propagate through the scattering medium (SM) and the single mode fiber (SF2) to reach PD2. The single mode fiber enables higher quality correction than previous quality assurance systems which use a camera to monitor the phase conjugation quality.
3. **Digitally search for tilt and shift misalignment (loop B).** To assess the respective contributions of the shift and tilt misalignment between the camera and the SLM, the phase conjugate solution was digitally shifted and tilted while monitoring the intensity of PD2. This allows the misalignment to be mapped out before physically correcting the misalignment. Although we can digitally correct for the shift and tilt, we prefer to correct these parameters physically to reduce the computational time and improve the system performance during TRUE focusing operation.
4. **Physically correct for the tilt and shift misalignment (loop B).** The tilt misalignment was corrected by tilting mirror M10 to maximize the signal captured by PD2. Similarly, the shift misalignment was corrected by translating the SLM in plane to maximize the detected signal on PD2.
5. **Aberration correction (loop B).** The aberration of the SLM, the playback (PB) beam, and the associated optics in the light-path were digitally corrected by adding a compensation phase map determined using a series of Walsh-Hadamard patterns (*76*). The compensation map was saved for later use during the TRUE focusing procedure.
6. **Aberration correction for the CW laser.** Since loop B was also used for the continuous-wave playback beam, a compensation phase map for this beam was measured as well. In this case, we switched the playback beam from the PW laser to the CW laser by switching the shutter BSS1.
7. **Alignment for DOPC loop A.** The PW laser was enabled again by flipping shutter BSS1. DOPC loop A was also enabled by flipping shutters BSS2 and BSS3. Steps 2 to 5 were repeated to align DOPC loop A. Since loop A travels a different optical path, the physical tilt and shift correction is distinct from that of loop B. For loop A we corrected the tilt misalignment by tilting beamsplitter BS4 and the shift misalignment by simultaneously tilting beamsplitters BS8 and BS4.

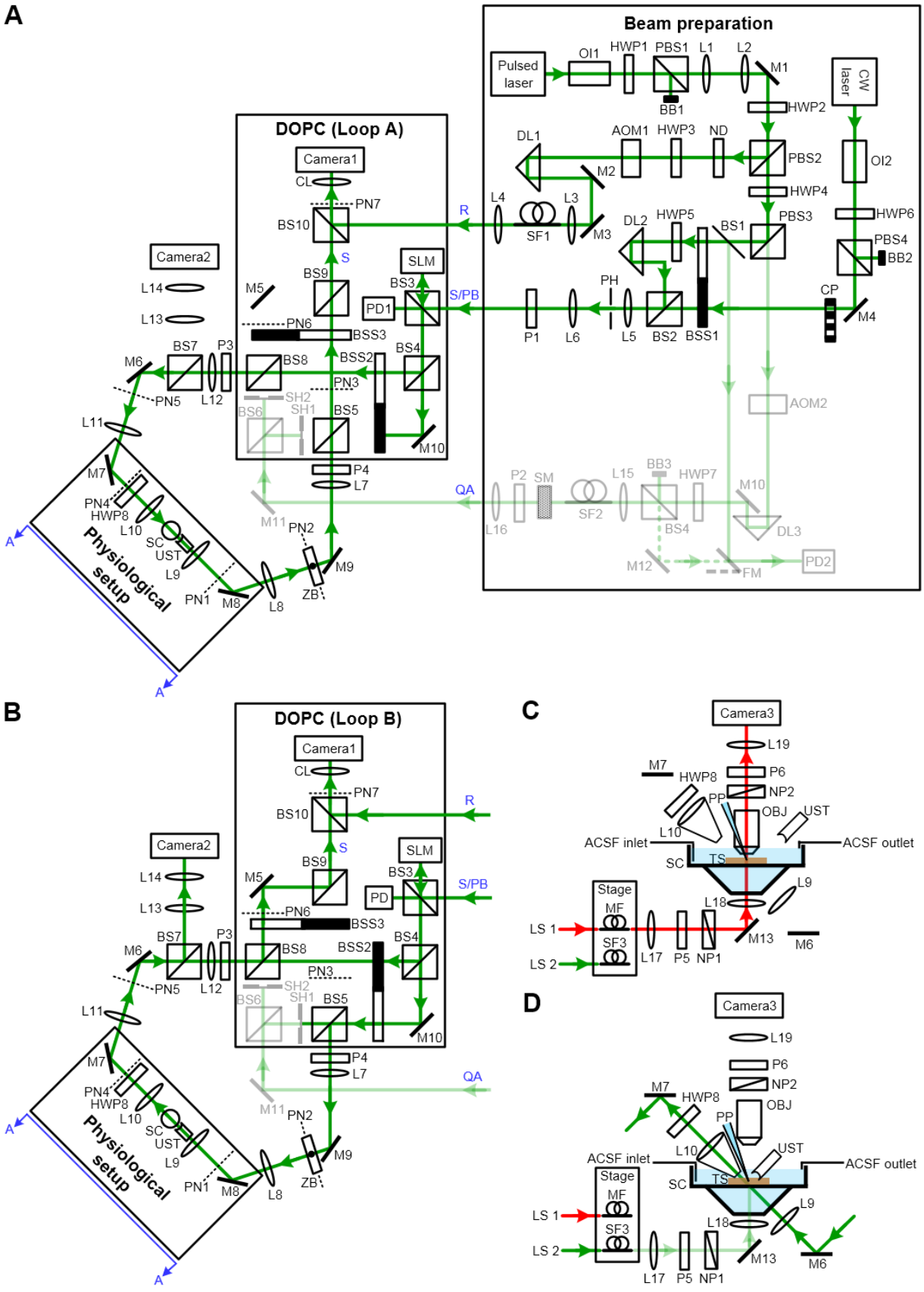
A
Beam preparation
Pulsed laser
OI1
HWP1
PBS1
L1
L2
M1
BB1
HWP2
CW laser
DL1
AOM1
HWP3
ND
PBS2
OI2
M2
HWP4
L4
L3
SF1
M3
DL2
HWP5
BS1
PBS3
HWP6
PBS4
BB2
PH
CP
M4
P1
L6
L5
BS2
BSS1
AOM2
DOPC (Loop A)
Camera1
CL
PN7
BS10
R
S
SLM
BS9
BS3
S/PB
PD1
M5
PN6
BSS3
Camera2
L14
L13
BS7
P3
BS8
BSS2
BS4
M6
PN5
L12
PN3
SH2
SH1
BS6
BS5
L11
M10
P4
L7
QA
M7
PN4
HWP8
L10
SC
UST
L9
PN1
M8
L8
ZB
M9
PN2
M11
P2
SM
L15
BB3
HWP7
SF2
L16
BS4
DL3
M12
FM
PD2
Physiological setup
A
B
DOPC (Loop B)
C
Camera3
L19
M7
HWP8
P6
NP2
PP
OBJ
UST
ACSF inlet
ACSF outlet
L10
SC
TS
L9
Stage
MF
L18
LS 1
SF3
M13
M6
LS 2
L17
P5
NP1
D

fig. S1. Setup. (**A** and **B**) Schematic of the setup for DOPC Loop A and Loop B. (**C**) The physiological setup (the A-A section in A and B) running in the neuron observation and patching mode. (**D**) The physiological setup running in the neuron stimulation mode. Abbreviations: ACSF, artificial cerebrospinal fluid; AOM, acousto-optic modulator; BB, beam block; BS, beamsplitter; BSS, beam selecting shutter; CL, camera lens; CP, chopper; CW laser, continuous-wave laser; DL, delay line; FM, flip mirror; HWP, half-wave plate; L, lens; LS, light source; M, mirror; MF, multi-mode fiber; ND, neutral-density filter; NP, Nomarski prism; OI, optical isolator; P, polarizer; PB, playback beam; PBS, polarizing beamsplitter; PD, photodiode; PH, pinhole; PN, plane; PP, pipette; QA, quality assurance; R, reference beam; S, sample beam; SC, sample chamber; SF, single-mode fiber; SH, optical shutter; SLM, spatial light modulator; SM, scattering medium; TS, tissue slice; UST, ultrasonic transducer; ZB, zeroth-order block (a black 100 μm-diameter disk printed on a transparency).

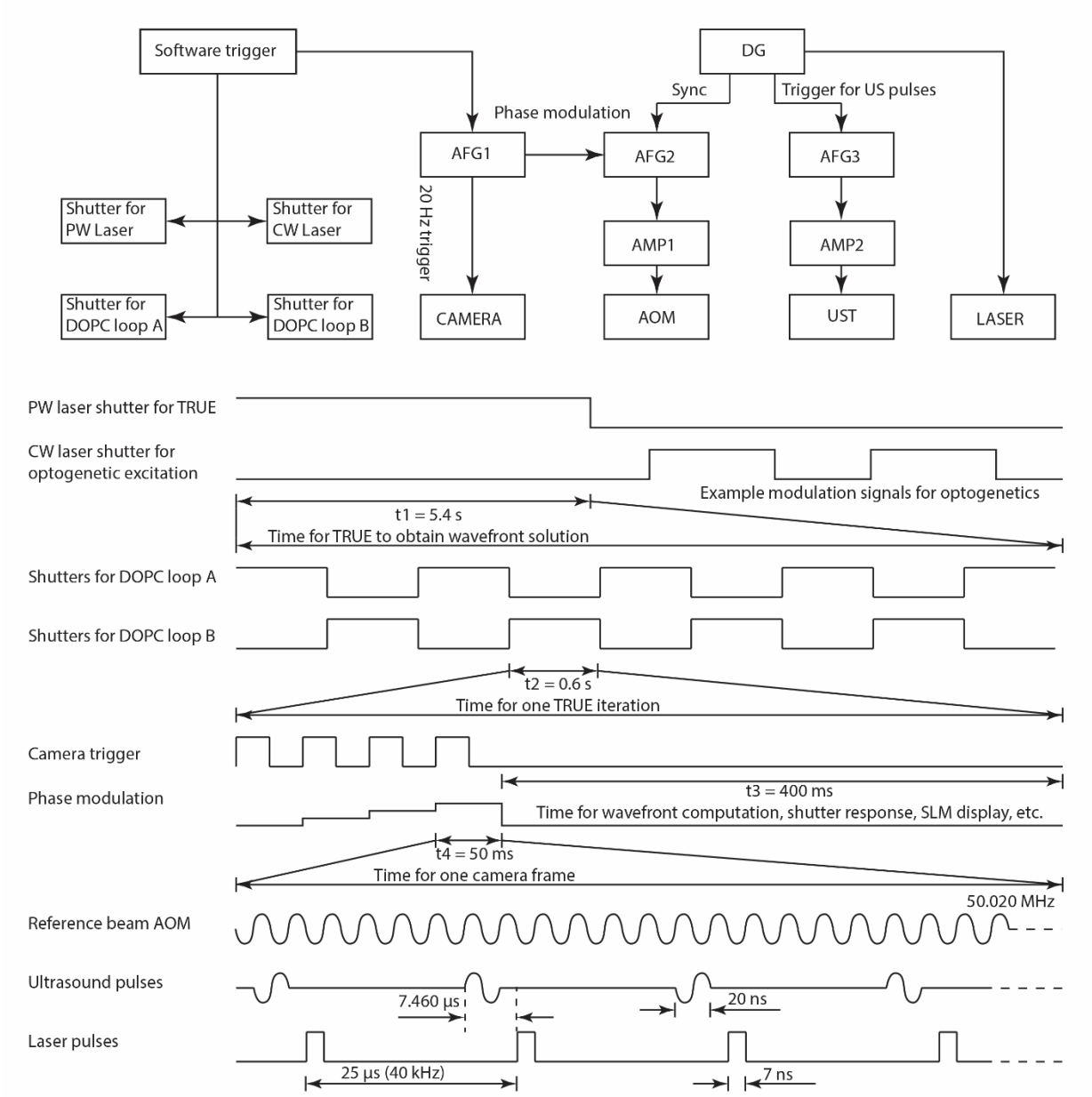

fig. S2. Electrical signal flow diagram. The experiment can be divided into two phases. In the first phase, the TRUE focusing system searches for the wavefront solution using a pulsed-wave (PW) laser. After that, we switch to a continuous-wave (CW) laser by controlling the shutters using software triggers. To obtain a correct wavefront solution, we implement nine iterations of the TRUE focusing process by switching the shutters that select between DOPC loop A and B. In each DOPC loop, a four-step phase-shifting holography approach is used to measure the optical field of the ultrasound modulated light. In this case, an arbitrary function generator (AFG1) is used to synchronize the camera and the phase of the reference beam. The frequency of the reference beam is shifted by 50.020 MHz by AFG2. The reference beam shares a clock with the ultrasound pulses and lasers pulses, both of which are triggered at 40 kHz. A 7.46 µs delay is used to compensate for the propagation time of the ultrasound wave traveling to the ultrasound focus. Abbreviations: AFG, arbitrary function generator; AMP, amplifier; AOM, acousto-optic modulator; DG, delay generator; UST, ultrasound transducer.

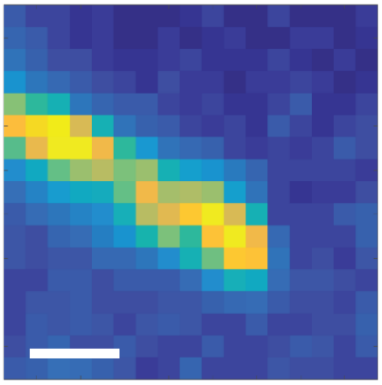

fig. S3. Ultrasound pulse-echo image of the tip of the glass pipette electrode. To focus ultrasound to the targeted neuron that is patch-clamped by the glass pipette, the ultrasound transducer is scanned to image the pipette tip in pulse-echo mode. The echo is recorded at each scanning position to form an image of the tip where the neuron is located. The transducer is then moved to that location so that the ultrasound focus overlaps with the neuron. Scale bar, 100 µm.

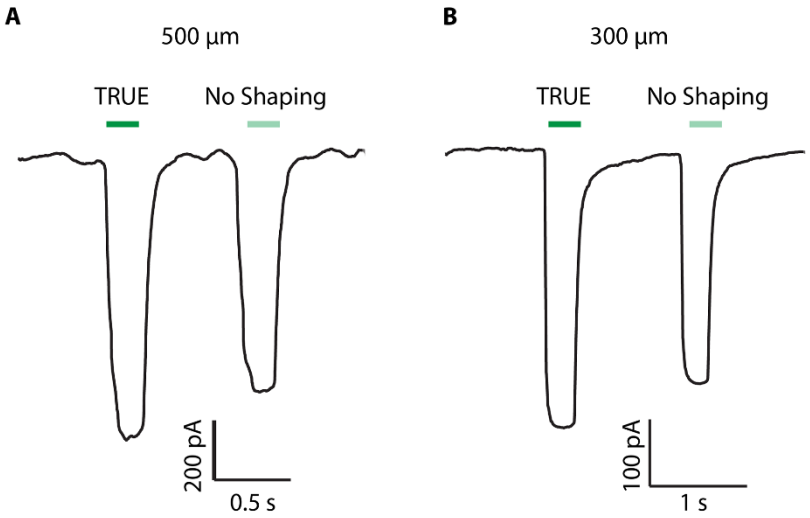

fig. S4. Electrophysiological photocurrent traces from neurons in 500- and 300-µm-thick acute brain slices. TRUE focusing enables photocurrent enhancement at depths of 500 µm (**A**) and 300 µm (**B**) in addition to the 800 µm thickness shown in the main text.

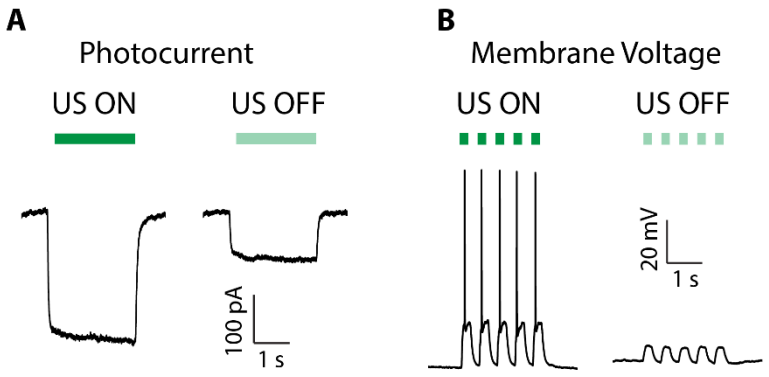

fig. S5. Electrophysiological photocurrent and membrane voltage traces comparing ultrasound on and off conditions. (**A**) Photocurrent traces when performing the TRUE focusing procedure with the ultrasound on and off. When the ultrasound is on, a phase map is measured which enables light to be focused to the location of the ultrasound focus and the neuron cell body. In contrast, when the ultrasound is disabled by turning off its driving amplifier, an incorrect phase map is measured so that the playback beam is not focused onto the neuron. As a result, we see a decrease in the amplitude of the photocurrent. (**B**) Membrane voltage traces when performing the TRUE focusing procedure with the ultrasound on and off. When the ultrasound is on, the playback beam is focused onto the neuron and elicit action potentials. In comparison, when the ultrasound is off, light is not focused onto the neuron and therefore no action potentials are elicited. It should be noted that the photocurrent and membrane voltage are lower with ultrasound off than those with ultrasound on followed by a shifted TRUE phase map displayed on the SLM (Fig. 3) which leads to an artificially increased photocurrent enhancement since the overall energy in the "US OFF" condition is lower than in the "No Shaping" condition. This is because the random phase map measured with ultrasound off has a higher spatial frequency (1/pixel size) than that of a normal phase map, and these high frequency components are filtered out by the limited numerical aperture of the optical system. In contrast, the shifted phase pattern in the "No Shaping" condition does not change the spatial frequency distribution of the phase map measured with ultrasound on and therefore maintains the same background intensity level as the background of the TRUE focus.